Available online at www.sciencedirect.com
ScienceDirect
Trans. Nonferrous Met. Soc. China 35(2025) 2061−2073
Transactions of Nonferrous Metals Society of China
www.tnmsc.cn

Effect of CaO and P_2O_5 on non-isothermal crystallization of alkaline vanadium slag

Can-can YU[1,2], Jiang DIAO[1,2], Jin-an WANG[1,2], Wen-feng TAN[1,2], Hong-yi LI[1,2], Bing XIE[1,2]

1. College of Materials Science and Engineering, Chongqing University, Chongqing 400044, China;
2. Chongqing Key Laboratory of Vanadium−Titanium Metallurgy and Advanced Materials, Chongqing University, Chongqing 400044, China

Received 14 November 2023; accepted 19 July 2024

Abstract: The phase composition and microstructure of alkaline vanadium slag were characterized using scanning electron microscopy and energy-dispersive X-ray spectroscopy (SEM−EDS) and X-ray diffraction (XRD). A crystallization model of spinel was established to calculate the effects of basicity (the mass ratio of CaO to SiO_2) and P_2O_5 on crystal growth rates and precipitation patterns. Based on the crystal size distribution (CSD) theory, the size distribution and growth mechanisms of spinel crystals in alkaline vanadium slag at different temperatures were investigated. The results revealed that, at a cooling rate of 5 K/min, the mean grain size of spinel increased from 12.77 to 21.52 μm as the temperature decreased from 1748 to 1598 K, with spinel growth being controlled by the interface. At 1548 K, the spinel particle size reached 31.04 μm, indicating a supply-controlled growth mechanism as the temperature decreased from 1598 to 1548 K. Increased P_2O_5 content hindered the crystal growth, while an increase in basicity promoted nucleation and growth. Furthermore, $MnCr_2O_4$ preferentially crystallized and grew in alkaline vanadium slag.
Key words: alkaline vanadium slag; CaO content; P_2O_5 content; spinel; crystallization; kinetics

1 Introduction

Vanadium (V), recognized as a strategic metal, finds extensive applications in industries ranging from steel production to high-temperature alloys, hydrogen storage alloys, redox flow batteries, and photocatalytic materials [1−4]. The primary source for vanadium extraction is vanadium−titanium magnetite, which undergoes a series of processes [5−7]. Initially, it is smelted in a blast furnace to yield vanadium-containing hot metal, subsequently oxidized in a converter to produce vanadium slag alongside semi-steel [8−10]. While semi-steel is further refined to obtain molten steel, vanadium slag is subjected to roasting and leaching procedures to obtain vanadium products [11]. The introduction of the calcification roasting-acid leaching process enables the incorporation of lime into the vanadium extraction converter, resulting in the production of alkaline vanadium slag. Unlike conventional industrial vanadium slag, which typically contains 1%−3% CaO with negligible P_2O_5 content, alkaline vanadium slag is characterized by higher CaO levels and increased P_2O_5 content [12]. These compositional differences lead to significant alteration in its physicochemical properties.

In vanadium slag, vanadium element is predominantly enriched in spinel phases, with a smaller fraction distributed within silicate phases [13]. The extraction efficiency of vanadium is influenced by the composition of the physical phases present in vanadium slag, spinel particle size,

Corresponding author: Jiang DIAO, Tel: +86-13983228181, E-mail: diaojiang@163.com
https://doi.org/10.1016/S1003-6326(25)66801-4

elemental distribution pattern, and subsequent roasting−leaching processes. CHEN and YANG [14] demonstrated the significant impact of spinel particle size on the vanadium oxidation rate during the roasting phase. Large spinel particle sizes are found to be advantageous in reducing the encapsulation of spinel by silicates, thereby enhancing the vanadium oxidation rate during roasting. The elevation in CaO and P_2O_5 content in alkaline vanadium slag inevitably induces alteration in the optimal thermodynamic conditions and kinetic laws governing the precipitation and growth of spinel phases. Consequently, it becomes imperative to monitor the variations in CaO and P_2O_5 content concerning the crystallization behavior of different phases during the condensation process of alkaline vanadium slag, particularly focusing on the crystallization process of spinel crystals.

In this work, the phase composition and distribution of spinel crystal sizes in alkaline vanadium slag were studied. Through the development of a mathematical model and crystallization kinetic experiments, the growth mechanism of the spinel phase in alkaline vanadium slag was elucidated. Additionally, the influence of CaO and P_2O_5 on spinel growth was examined, offering valuable insights for optimizing subsequent vanadium extraction processes.

2 Experimental

2.1 Materials

The composition of industrial vanadium slag was adjusted to design five groups of vanadium slags with varying CaO contents (R1−R5) and five groups with different P_2O_5 contents (P1−P5). The specific compositions of the samples are listed in Table 1. Notably, R1 represents the industrial vanadium slag, while vanadium slag P5 was prepared for high-temperature melt calcination. Prior to weighing, the CaO reagent underwent calcination in a $MoSi_2$ furnace at 1273 K for 12 h to decompose all carbonate impurities. Vanadium slag P5 was prepared by combining (40±0.01) g of industrial slag with additional $Ca_3(PO_4)_2$ (99 wt.%) and CaO (99 wt.%) based on the vanadium slag compositions listed in Table 1.

2.2 Experimental procedure

Vanadium slag P5 from Table 1 was thoroughly mixed and melted in a $MoSi_2$ furnace, as depicted in Fig. 1. The experimental setup included the following steps: The raw materials were mixed and dried in a drying oven for 12 h at 378 K. Subsequently, the dried samples were loaded into a pure iron crucible and then placed in a corundum crucible. Upon reaching the target temperature, argon was introduced to purge the air from the furnace, and the crucible was inserted into the $MoSi_2$ furnace. The experiments were conducted under an argon atmosphere, with the temperature gradually increasing to 1748 K and maintained for 30 min before being cooled at a rate of 5 K/min. At temperatures of 1748, 1698, 1648, 1598 and 1548 K, the slag samples in the crucible were glued with Mo rods and swiftly immersed in water to facilitate rapid cooling, thereby preserving the high-temperature structure. The water-quenched slags were initially embedded in organic resin, followed by successive abrasion of the specimen

Table 1 Chemical compositions of different vanadium slags (wt.%)

No.	MgO	Fe_2O_3	V_2O_3	MnO	TiO_2	SiO_2	P_2O_5	CaO	Cr_2O_3	Al_2O_3	Other	*R*
R1	2.12	34.57	14.18	7.27	13.73	13.96	0.08	2.47	6.92	3.40	1.30	0.18
R2	1.97	32.16	13.19	6.76	12.77	12.99	1.14	8.21	6.44	3.16	1.21	0.63
R3	1.84	30.06	12.33	6.32	11.94	12.14	2.06	13.20	6.02	2.96	1.13	1.09
R4	1.70	27.66	11.34	5.82	10.98	11.17	2.81	19.23	5.54	2.72	1.04	1.72
R5	1.54	25.14	10.31	5.29	9.99	10.15	3.39	25.74	5.03	2.47	0.95	2.54
P1	1.79	29.17	11.97	6.14	11.59	11.78	0.07	17.70	5.84	2.87	1.10	1.50
P2	1.76	28.63	11.74	6.02	11.37	11.56	1.96	17.33	5.73	2.82	1.08	1.50
P3	1.69	27.49	11.28	5.78	10.92	11.10	5.80	16.70	5.50	2.70	1.03	1.50
P4	1.63	26.59	10.91	5.59	10.56	10.74	8.87	16.17	5.32	2.62	1.00	1.50
P5	1.58	25.80	10.58	5.43	10.25	10.42	11.68	15.59	5.16	2.54	0.97	1.50

R: Basicity

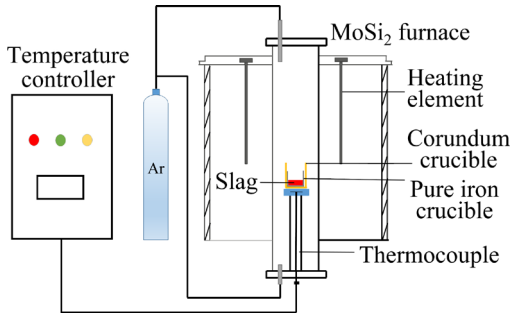

Fig. 1 Schematic diagram of experimental apparatus

surfaces using SiC sandpaper with mesh sizes ranging from 200 to 2000. Post-abrasion, the surfaces of the slag samples were cleaned by agitation in an ultrasonic cleaner filled with alcohol for 15 min. Subsequently, the slag samples were removed, dried, and examined using scanning electron microscopy (SEM, Thermo Fisher Scientific, USA) with energy-dispersive spectroscopy (EDS).

During SEM observation, five random fields of view were selected for each specimen to capture microscopic images of the slag samples. The morphology and distribution of spinel in the slag were documented and utilized for subsequent statistical analysis. The SEM images obtained under various experimental conditions were utilized to measure the grain size and area of spinel in different fields of view.

2.3 Theoretical calculation

According to the classic crystallization kinetic model reported by TURNBULL [15], the nucleation rate (I) can be expressed as

$$I=\frac{N_{\mathrm{v}}kT}{3\pi a^3\eta}\exp\left[\frac{-16\pi\alpha^3\beta}{3T_{\mathrm{r}}\left(\Delta T_{\mathrm{r}}\right)^2}\right] \tag{1}$$

where k is the Boltzmann's constant, T is the temperature, a is the lattice parameter of the crystal, N_{v} is the number of molecules (or atoms) per unit volume, η is the viscosity, α is the reduced crystal/liquid interfacial tension, β is the reduced molar heat of fusion (values of α and β are referenced from Ref. [15], in which good accordance with experimental results was achieved, i.e., the value of α is 1/3 and β is 1), T_{r} denotes temperature, and ΔT_{r} denotes subcooling.

The viscosity of vanadium slag was obtained by the Urbain viscosity model [16], which is a two-parameter expression for viscosity and can be expressed as follows:

$$\eta_0=AT\exp(1000B/T) \tag{2}$$

where A is a modified pre-exponential parameter, and B is a parameter related to network forming agents, network modifier and amphoteric in this system.

The model classifies the components in the slag into three categories: network forming agents, network modifier and amphoteric. In this work, the sum of the mole fractions of the different types of slag components was calculated and classified according to the composition of the slag system. Network forming agents include SiO_2 and P_2O_5, network modifier includes MnO, MgO, CaO, TiO_2, and V_2O_3, and amphoteric includes Al_2O_3, Fe_2O_3, and Cr_2O_3.

The relation between A and B can be calculated by

$$-\ln A=0.2693B+11.6725 \tag{3}$$

$$B=B_0+B_1X_{\mathrm{G}}+B_2X_{\mathrm{G}}^2+B_3X_{\mathrm{G}}^3 \tag{4}$$

where B_0, B_1, B_2 and B_3 are all related to X_{A} and X_{M} [16], and X_{A}, X_{M} and X_{G} are the mole fractions of the network forming agents, network modifier oxides and amphoteric oxides, respectively.

However, the molten vanadium slag at 1623−1773 K belongs to non-Newtonian fluids, and the description of the viscosity of non-Newtonian fluids is in accordance with the Einstein−Roscoe equation as [17,18]

$$\eta=\eta_0\left(1-m^*\phi_{\mathrm{s}}\right)^{-n} \tag{5}$$

where η and η_0 represent the viscosity of the non-homogeneous fluid and residual liquid in the absence of solid particles, respectively; m^* and n are empirical parameters, and the values of m^* and n are 1 and 2.5, respectively; ϕ_{s} is the volume fraction of solid particles, and it can be obtained from Eq. (6) [19]:

$$\phi_{\mathrm{s}}=\frac{V_{\mathrm{s}}}{V_{\mathrm{s}}+V_{\mathrm{L}}};\ V_{\mathrm{S}}=\sum_j v_j^{(\mathrm{S})}\frac{m_j^{(\mathrm{S})}}{M_j};\ V_{\mathrm{L}}=\sum_i v_i^{(\mathrm{L})}\frac{m_i^{(\mathrm{L})}}{M_i} \tag{6}$$

where V_{S} and V_{L} represent the volumes of the solid and residual liquid phases, respectively, and the compositional contents of the residual liquid phase and solid particles in the slag were obtained by the Equilib module of the thermodynamic software

FactSage 8.1, with the reaction databases FactPS and FToxid selected; m, v and M represent the mass, partial molar volume, and relative molecular mass of the liquid phase component i or the solid phase component j, respectively. Due to the lack of partial molar volume values for the components, the value of m was replaced using the average molar volume value, which was calculated by FactSage 8.1. The results are listed in Table 2.

Table 2 Average molar volume of components ($cm^3 \cdot mol^{-1}$)

Al_2O_3	SiO_2	CaO	FeO	Fe_2O_3	MgO
25.68	22.68	16.76	12.25	30.26	11.25
MnO	CrO	Cr_2O_3	Ti_2O_3	TiO_2	Mn_2O_3
13.02	19.19	29.17	31.25	18.81	35.08
Fe_3O_4	$Ca_3(PO_4)_2$	$FeCr_2O_4$	$MgCr_2O_4$	$CaTiO_3$	
44.52	98.78	45.04	41.80	33.16	

The growth rate, denoted as U, is determined in a similar fashion [20].

$$U=\frac{fkT}{3\pi a^2\eta}\left[1-\exp\left(\frac{-\beta\cdot\Delta T_r}{T_r}\right)\right] \tag{7}$$

$$f=\begin{cases}1, \ \Delta H_m<2RT_m\\ 0.2\Delta T_r, \ \Delta H_m\geq 4RT_m\end{cases} \tag{8}$$

where ΔH_m is the molar heat of fusion, R is the molar gas constant, T_m is the melting point of crystal, and f is the fraction of acceptor sites on the crystal surface.

3 Results and discussion

3.1 Morphological changes of alkaline vanadium slag during cooling and crystallization

Figure 2 displays the XRD pattern of P5 vanadium slag, revealing the predominant phases as the spinel phase and silicate phase. Additionally, Fig. 3 shows the SEM morphology of P5 vanadium slag at temperatures ranging from 1748 to 1548 K, with a cooling rate of 5 K/min. The results were further analyzed by EDS point scanning at various locations, as detailed in Table 3. As the temperature decreases from 1748 to 1548 K, a notable growth and aggregation process is observed in the morphological features of spinel. Initially, at 1748 K, the spinel exhibits small size and relatively scattered distribution, indicating a low nucleation and growth rate. However, as the temperature decreases further, the smaller spinels collide and merge to form larger aggregates, either by direct annexation to existing large spinel particles or through independent nucleation and growth processes. Furthermore, the EDS analysis presented in Table 3 highlights the concentration of V, phosphorus (P), and titanium (Ti) primarily within the white spinel phase, while silicon (Si) and calcium (Ca) are predominantly concentrated in the dark grey silicate phase. Additionally, iron (Fe) and magnesium (Mg) are found to be distributed in both phases.

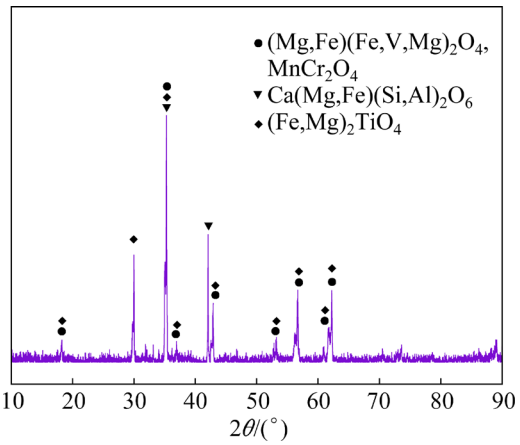

Fig. 2 XRD pattern of P5 vanadium slag

Figure 4 illustrates the mean particle size of spinel from samples rapidly cooled. At a cooling rate of 5 K/min, there is a noticeable growth trend of spinel as the temperature decreases from 1748 to 1598 K, with the mean particle size increasing from 12.77 to 21.52 μm. Further decrease in temperature results in accelerated spinel growth, with the grain size reaching 31.04 μm at 1548 K. The average spinel size of the alkaline vanadium slag studied in this study was 30.00 μm when continuously cooled from 1748 to 1548 K at 5 K/min. In contrast, the mean spinel size of industrial vanadium slag, cooled from 1673 to 1523 K at the same rate, was only 23.50 μm [21]. This discrepancy suggests that the high CaO content in the vanadium slag favors spinel growth. Moreover, another alkaline vanadium slag with slightly different composition content, cooled from 1723 to 1523 K at 5 K/min, exhibited a mean spinel particle size of 36.44 μm [22]. This further supports the notion that high CaO content promotes spinel growth within a variation range of up to 17.52 wt.%.

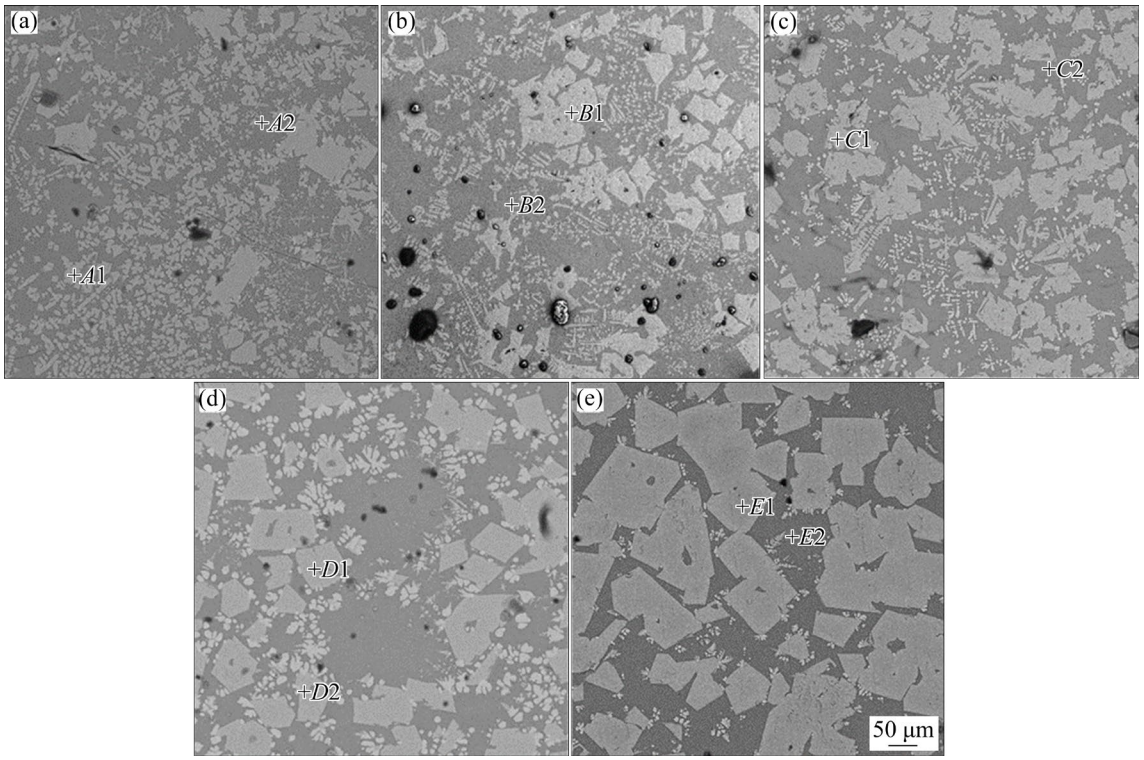

Fig. 3 SEM images of P5 vanadium slag at 1748 K (a), 1698 K (b), 1648 K (c), 1598 K (d), and 1548 K (e)

Table 3 EDS results of P5 vanadium slag showing different areas in Fig. 3 (at.%)

Area	Phase	O	Fe	V	P	Cr	Ti	Si	Ca	Mn	Al	Mg
*A*1	Spinel	41.07	25.29	11.58	−	6.25	5.24	0.54	0.92	4.10	3.91	1.08
*A*2	Silicate	57.18	7.62	0.34	−	−	2.55	12.54	15.31	1.67	1.84	0.95
*B*1	Spinel	65.65	11.11	7.26	−	4.70	2.53	0.35	0.49	1.31	3.93	2.67
*B*2	Silicate	69.65	3.60	0.07	−	0.32	0.55	13.20	9.57	0.51	2.11	0.42
*C*1	Spinel	70.06	11.88	2.31	−	0.64	5.36	1.95	1.23	1.55	2.80	2.24
*C*2	Silicate	71.46	2.33	0.47	−	−	0.99	12.73	9.32	0.48	1.49	0.71
*D*1	Spinel	38.05	23.54	13.40	−	9.15	6.12	0.44	0.70	3.21	3.06	2.31
*D*2	Silicate	58.69	9.90	−	−	−	1.48	13.74	11.95	1.76	1.71	0.79
*E*1	Spinel	42.99	19.15	12.08	−	7.53	4.51	−	0.15	3.53	6.60	3.46
*E*2	Silicate	53.39	8.94	0.24	−	−	1.62	16.03	15.68	1.62	1.40	1.08

3.2 Non-isothermal crystallization kinetics of spinel crystals

The crystal size distribution (CSD) theory was used to analyze the growth mechanism and limiting links of spinel in alkaline vanadium slag [23,24]. The lognormal distribution function of the CSD curve for the lognormal distribution type is Eq. (9), which is used to describe the distribution of crystal size.

$$f(D)=\frac{1}{D\beta\sqrt{2\pi}}\exp[-(\ln D-\alpha)^2/(2\beta^2)] \quad (9)$$

where D represents the grain size of the crystal; $f(D)$ represents the frequency of occurrence when the grain size of the crystal is D; α and β^2 represent the mean and variance of the lognormal distribution function, respectively.

Figure 5 depicts the CSD curve of spinel in P5 vanadium slag at a cooling rate of 5 K/min. In the temperature range of 1598−1748 K, the CSD curve exhibits an approximately normal distribution shape, suggesting that spinel growth is primarily controlled by the interface. During this temperature

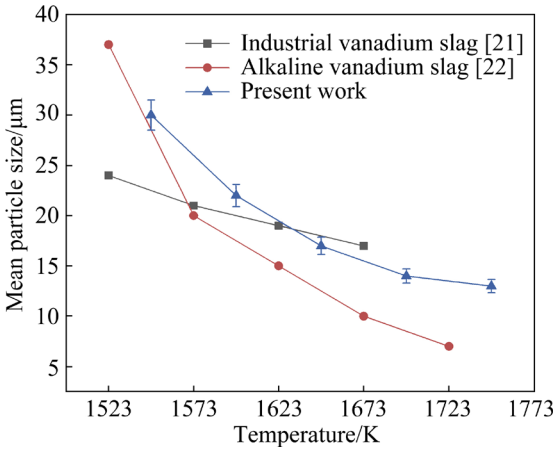

Fig. 4 Mean particle size of spinel versus temperature at cooling rate of 5 K/min

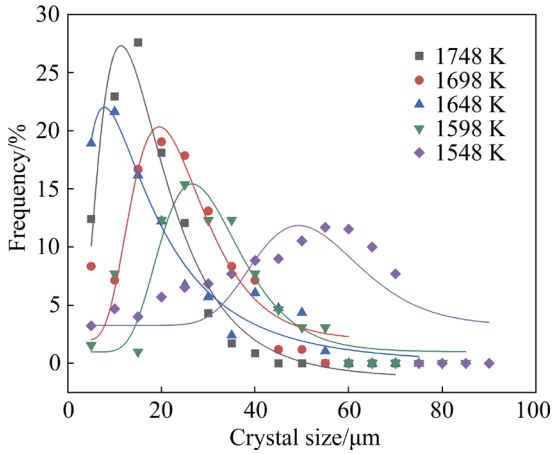

Fig. 5 Crystal size distribution of spinel at different temperatures

range, the vanadium slag exists in a molten state with sufficient mobility, and there is significant subcooling, leading to a crystal growth process primarily characterized by the adsorption of new atoms at the solid−liquid phase interface. As the temperature decreases from 1598 to 1548 K, the CSD curve transitions to an Ostwald ripening type, indicating that the spinel growth mechanism shifts to supply-controlled. This shift is attributed to the increase in slag viscosity with decreasing temperature, which restricts the mass transfer and diffusion of liquid-phase components. The crystallization kinetics of crystals during crystallization can be inferred from the relationship between α and β^2 when the CSD curve follows a lognormal distribution. As shown in Fig. 6, for alkaline vanadium slag at a cooling rate of 5 K/min, β^2 exhibits a linear increase with α, indicating that spinel growth is governed by interfacial growth. Similarly, for industrial vanadium slag [21], where the cooling rate is 5 K/min, spinel growth is also controlled by the interface due to the prolonged residence time in the high-temperature section facilitating diffusion.

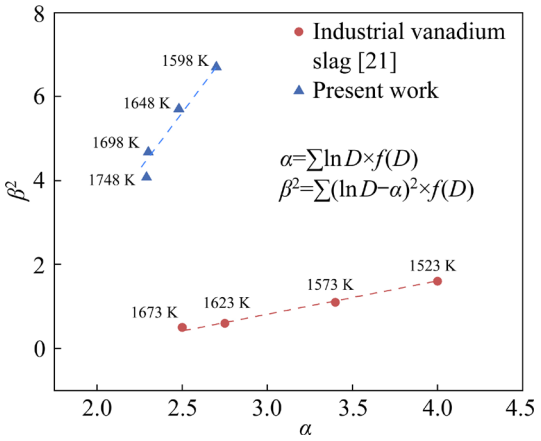

Fig. 6 Relationship between α and β^2 at different temperatures for P5 slag samples at cooling rate of 5 K/min

3.3 Effect of CaO content on crystal crystallization

According to the XRD pattern of Fig. 2, the main crystals of P5 vanadium slag are FeV_2O_4, MgV_2O_4, Fe_2TiO_4, Mg_2TiO_4, $MnCr_2O_4$, $CaMgSi_2O_6$, and $CaFeSi_2O_6$, and the structural parameters and melting point of these crystals are shown in Table 4.

Table 4 Parameters of crystals used in calculation

Crystal	a/Å	N_v/m^{-3}	T_m/K
FeV_2O_4	8.543 [25]	1.604×10^{-27}	2023 [26]
MgV_2O_4	8.432 [27]	1.675×10^{-27}	2293 [28]
Fe_2TiO_4	8.529 [29]	1.612×10^{-27}	1668 [30]
Mg_2TiO_4	8.472 [29]	1.645×10^{-27}	2029 [31]
$MnCr_2O_4$	8.437 [32]	1.665×10^{-27}	2970 [28]
$CaFeSi_2O_6$	10.089 [33]	9.738×10^{-28}	1423 [28]
$CaMgSi_2O_6$	7.598 [34]	2.280×10^{-27}	1664 [28]

Figure 7 illustrates the variations in nucleation rate (I) and growth rate (u) of crystals with increasing temperature at different levels of basicity. The temperatures corresponding to the peaks of the nucleation and growth rate curves signify the optimal nucleation and growth temperatures, collectively constituting the optimal temperature range for crystalline growth. It is observed that the optimal nucleation temperatures of each crystal are

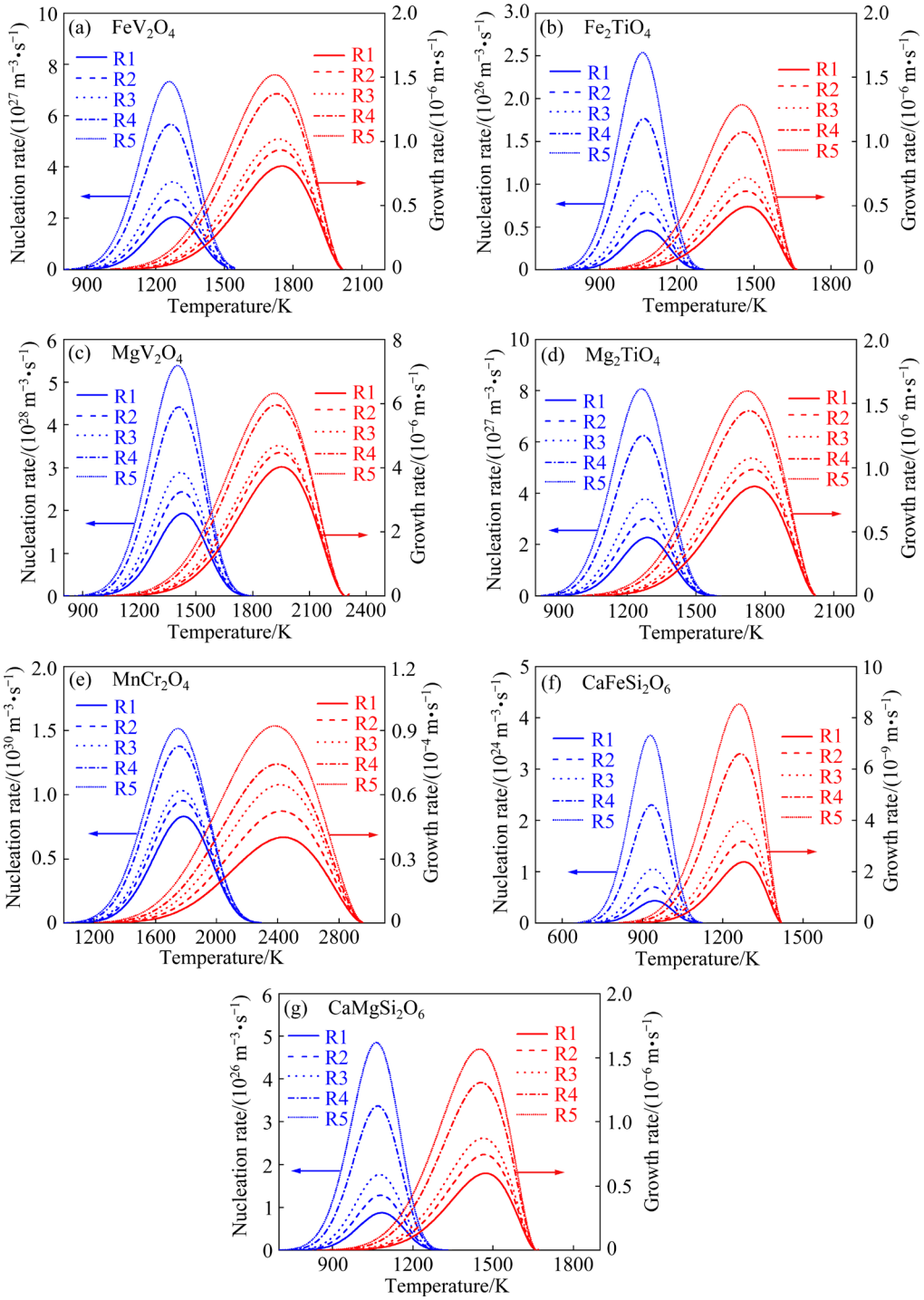

Fig. 7 Relationship between temperature and nucleation rate and growth rate of different crystals at different basicities

lower than the optimal growth temperatures. This is attributed to the fact that the driving force for nucleation mainly arises from the degree of subcooling. As the subcooling degree increases, the nucleation rate gradually rises, facilitating the generation of a larger number of smaller-sized crystal particles. Conversely, lower subcooling degrees are conducive to enhanced mass transfer and diffusion of liquid-phase components, resulting in higher growth rates and favoring crystal growth. As the CaO content increases from 2.47 to 25.74 wt.% (basicity increasing from 0.18 to 2.54), the nucleation and growth rates of the crystals exhibit an upward trend. This indicates that higher basicity levels are advantageous for nucleation and crystal growth, with the nucleation rate significantly

surpassing the growth rate. Furthermore, the nucleation and growth rates of $MnCr_2O_4$ are notably higher than those of other crystals, suggesting that $MnCr_2O_4$ will preferentially crystallize and grow in alkaline vanadium slag.

Table 5 presents the nucleation and growth temperature ranges for each crystal of R series slags. The close agreement between the nucleation and growth temperature intervals of FeV_2O_4 and Mg_2TiO_4 can be attributed to their similar melting points, 2023 and 2029 K, respectively. Similarly, the proximity in the nucleation and growth temperature intervals of Fe_2TiO_4 and $CaMgSi_2O_6$ is due to their close melting points, 1668 and 1664 K. In contrast, $CaFeSi_2O_6$ exhibits the lowest melting point among the crystals, at 1423 K, resulting in the smallest values for both endpoints of the nucleation and growth temperature intervals. Conversely, $MnCr_2O_4$ possesses the highest melting point, nearing 3000 K. Not only does it have the largest values for both endpoints of the nucleation and growth temperature intervals, but it also spans a wider range.

Table 5 Temperature range for each crystal of R series slags

Crystal	Nucleation temperature/K	Growth temperature/K	Optimal temperature for crystalline growth/K
FeV_2O_4	800−1545	1000−2020	1255−1720
Fe_2TiO_4	720−1300	900−1660	1065−1450
MgV_2O_4	890−1780	1090−2290	1405−1915
Mg_2TiO_4	850−1590	1000−2020	1260−1720
$MnCr_2O_4$	1050−2250	1200−3000	1750−2390
$CaFeSi_2O_6$	640−1130	820−1420	925−1260
$CaMgSi_2O_6$	710−1300	900−1660	1065−1450

The total crystallization rate r can be expressed as [35]

$$r = \frac{\pi}{3} IU^3 \tag{10}$$

The total crystallization rate for all crystals is shown in Eq. (11):

$$r_{\text{total}} = \sum_i w_i r_i \tag{11}$$

where r_i is the crystallization rate of a given crystal, and w_i is its mass fraction.

Figures 8(a−e) depict the variation of the integrated crystallization rate of each crystal with increasing temperature at different levels of basicity. As the basicity increases from 0.18 to 2.54, the integrated crystallization rate exhibits a significant increase across all crystals. Specifically, the integrated crystallization rate escalates by three orders of magnitude for $CaFeSi_2O_4$, two orders of magnitude for FeV_2O_4, Fe_2TiO_4, Mg_2TiO_4, and $CaMgSi_2O_4$, and one order of magnitude for MgV_2O_4 and $MnCr_2O_4$. At each level of basicity, $MnCr_2O_4$ crystals consistently exhibit the largest integrated crystallization rate, while $CaFeSi_2O_4$ crystals display the smallest one. In Fig. 8(f), the integrated crystallization rate of total crystals versus temperature at different basicities is illustrated. With an increase in basicity, there is a noticeable shift of the integrated crystallization rate of each crystal and the peak temperature of the integrated crystallization rate of total crystals towards lower temperatures. Consequently, the optimal crystallization temperature of the total crystals decreases from 2045 to 2000 K, indicating that higher basicity levels promote crystal growth. This phenomenon can be attributed to the reduction in slag viscosity and increase in the diffusion rate of liquid-phase components in the slag as basicity increases. Furthermore, the escalation in subcooling enhances the diffusion rate of liquid-phase components and improves the crystallization kinetics of crystals in alkaline vanadium slag. The peak temperatures of the total crystals and $MnCr_2O_4$ coincide, indicating that the optimal crystallization temperature of total crystals in alkaline vanadium slag is dependent on the crystal with the highest melting point, $MnCr_2O_4$.

3.4 Effect of P_2O_5 content on crystal crystallization

Figure 9 illustrates the variations in nucleation and growth rates of crystals with increasing temperature at different P_2O_5 contents. It is observed that the optimal nucleation temperatures of the crystals are lower than their optimal growth temperatures, and the nucleation rates significantly exceed the growth rates. As the P_2O_5 content increases from 0.06 to 11.68 wt.%, the nucleation and growth rates of the crystals exhibit a decline. This trend suggests that higher P_2O_5 content is not conducive to crystal growth in vanadium slag.

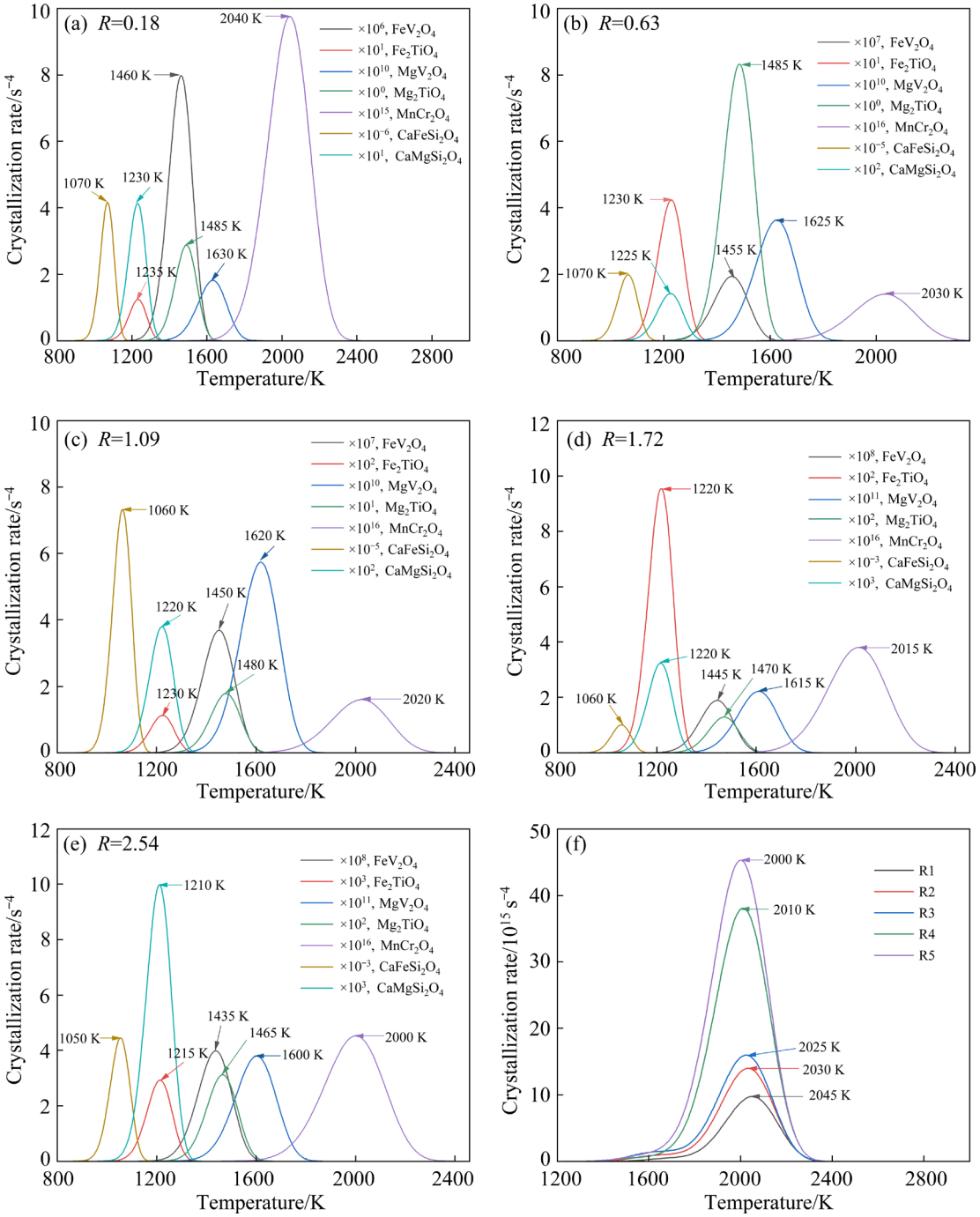

Fig. 8 Relationship between total crystallization rate and temperature at different basicities

Furthermore, the nucleation and growth rates of $MnCr_2O_4$ surpass those of other crystals, indicating its preferential crystallization and growth in alkaline vanadium slag with increased P_2O_5 content.

Table 6 displays the range of nucleation and growth temperatures for each crystal of P series slags. The nucleation and growth temperature ranges of each crystal closely mirror those observed with changes in basicity. This suggests that alterations in composition have minimal impact on the nucleation and growth temperature ranges of the crystals. Instead, the melting point of the crystals emerges as the decisive factor influencing the nucleation and growth temperature ranges.

Figures 10(a−e) depict the variation of crystallization rate with increasing temperature for each crystal at different P_2O_5 contents. As the P_2O_5 content increases from 0.06 to 11.68 wt.%, there is a notable decrease in the integrated crystallization rate of $CaFeSi_2O_6$ by three orders of magnitude,

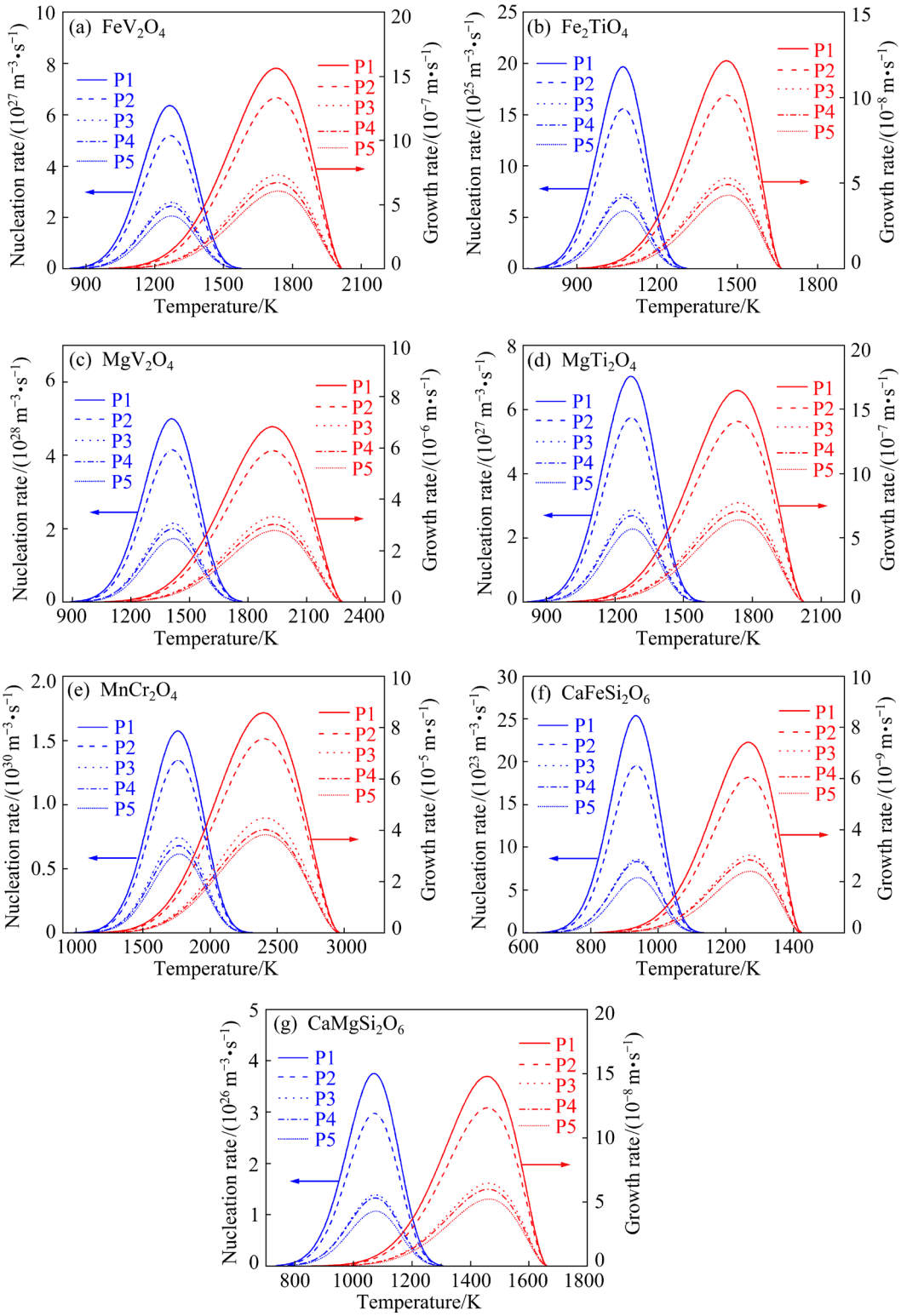

Fig. 9 Relationship between temperature and nucleation rate and growth rate of different crystals at different P_2O_5 contents

while that of FeV_2O_4, Fe_2TiO_4, MgV_2O_4, Mg_2TiO_4, and $CaMgSi_2O_6$ decreases by two orders of magnitude, and that of $MnCr_2O_4$ decreases by one order of magnitude. In Fig. 10(f), the integrated crystallization rate of total crystals in vanadium slag is plotted as a function of temperature for different P_2O_5 contents. It is observed that both the peak temperature of the integrated crystallization rate of each crystal and the integrated crystallization rate of total crystals shift to higher temperatures with

Table 6 Temperature range for each crystal of P series slags

Crystal	Nucleation temperature/K	Growth temperature/K	Optimal temperature for crystalline growth/K
FeV_2O_4	830−1580	1000−2010	1265−1725
Fe_2TiO_4	735−1315	900−1665	1070−1460
MgV_2O_4	900−1770	1090−2290	1410−1935
Mg_2TiO_4	820−1590	1000−2020	1270−1730
$MnCr_2O_4$	1000−2300	1200−2960	1760−2400
$CaFeSi_2O_6$	655−1130	820−1420	935−1260
$CaMgSi_2O_6$	745−1300	900−1660	1065−1460

increasing P_2O_5 content. Specifically, the peak temperature increases from 2010 to 2030 K. This phenomenon is attributed to the increase in viscosity of the vanadium slag with higher P_2O_5 content, which hampers mass transfer and diffusion during the crystallization process. Remarkably, the optimum crystallization temperature of the total crystals aligns closely with that of $MnCr_2O_4$, and the total crystallization rate of $MnCr_2O_4$ remains the highest at each P_2O_5 content. This suggests that the total crystallization rate of all crystals in the vanadium slag is primarily determined by the highest melting point of $MnCr_2O_4$.

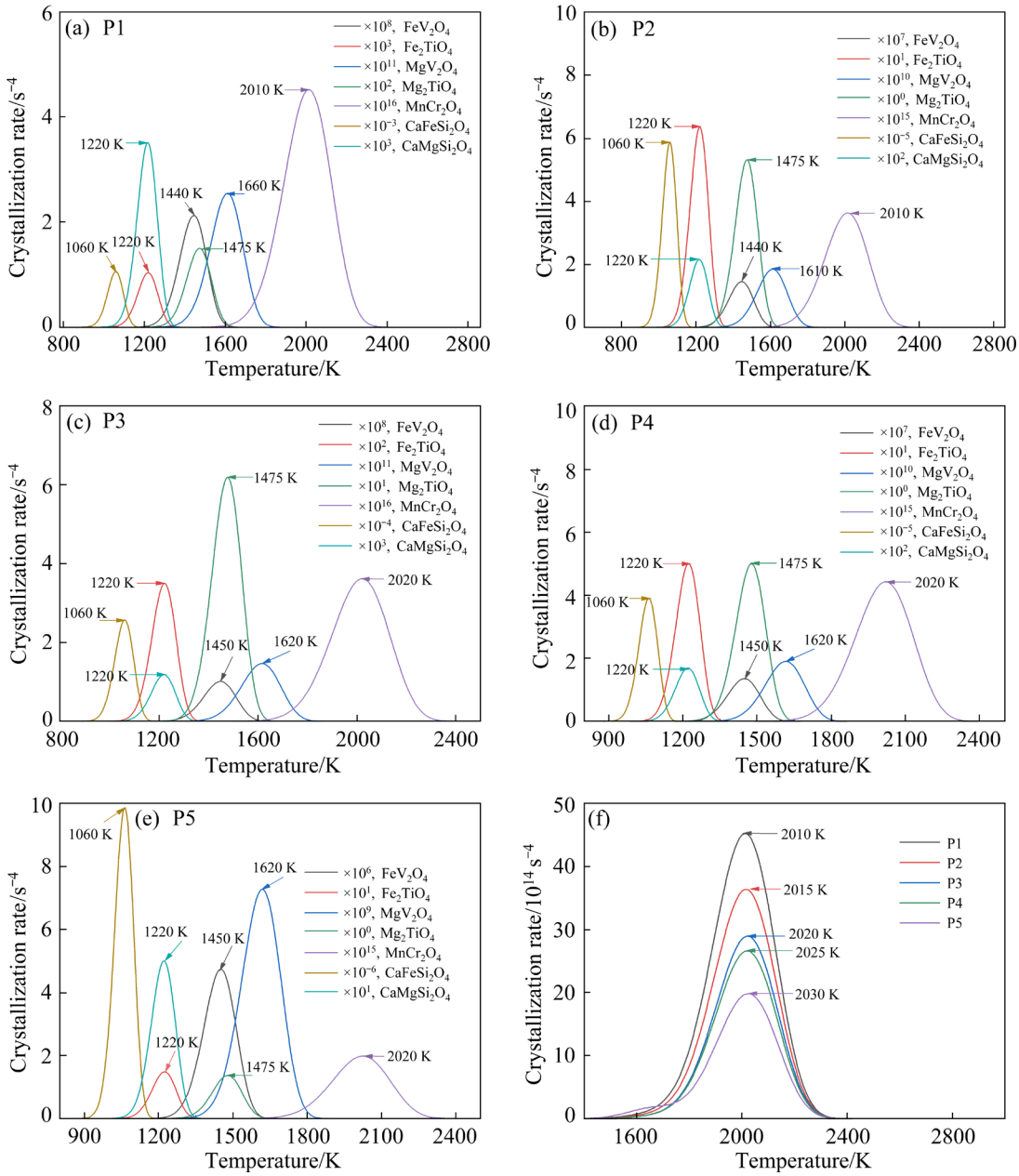

Fig. 10 Relationship between total crystallization rate and temperature at different P_2O_5 contents

4 Conclusions

(1) The primary phases present in alkaline vanadium slag are spinel and silicate phases. Upon decreasing temperature from 1748 to 1548 K, there is notable growth and aggregation observed in the morphological features of spinel. V, P, and Ti are predominantly concentrated in the spinel phase, while Si and Ca are primarily found in the silicate phase. Fe and Mg are distributed in both phases.

(2) At a cooling rate of 5 K/min, the mean particle size of spinel increases from 12.77 to 21.52 μm as the temperature decreases from 1748 to 1598 K. Further temperature reduction leads to accelerated spinel growth, with the grain size reaching up to 31.04 μm at 1548 K. The presence of high CaO content in vanadium slag favors spinel growth. Moreover, higher CaO content enhances spinel growth within a variation range of not exceeding 17.52 wt.%.

(3) Within the temperature range of 1598–1748 K and 1548−1598 K, spinel growth is governed by the interface and supply, respectively. At a cooling rate of 5 K/min, interfacial growth governs spinel growth in both alkaline and industrial vanadium slags.

(4) As the CaO content increases from 2.47 to 25.74 wt.% (basicity from 0.18 to 2.54), the nucleation rate and growth rate of crystals escalate. Simultaneously, the peak temperature of both the integrated crystallization rate of each crystal and the integrated crystallization rate of total crystals tend to shift to lower temperatures. Heightened basicity fosters crystal growth, while increasing the P_2O_5 content (from 0.06 to 11.68 wt.%) has the opposite effect. The optimum temperature of all crystals in alkaline vanadium slag hinges on the crystal with the highest melting point, $MnCr_2O_4$.

CRediT authorship contribution statement

Can-can YU: Investigation, Methodology, Writing − Origin draft, Writing − Review & editing; **Jiang DIAO:** Investigation, Conceptualization, Funding acquisition, Supervision, Writing − Review & editing; **Jin-an WANG:** Data curation, Writing − Review & editing; **Wen-feng TAN:** Investigation, Resources; **Hong-yi LI** and **Bing XIE:** Resources, Project administration.

Declaration of competing interest

The authors declare that they have no known competing financial interests or personal relationships that could have appeared to influence the work reported in this paper.

Acknowledgments

This work was supported by the National Natural Science Foundation of China (No. 51974047), the Natural Science Foundation of Chongqing, China (No. cstc2022ycjh-bgzxm0003), and the Large Instrument Foundation of Chongqing University, China (No. 202303150239).

References

[1] CHOI C, KIM S, KIM R, CHOI Y, KIM S, JUNG H Y, YANG J H, KIM H T. A review of vanadium electrolytes for vanadium redox flow batteries [J]. Renewable and Sustainable Energy Reviews, 2017, 69: 263−274.

[2] YANG Ming-e, YANG Hao-xiang, TIAN Sheng-hui, WANG Ming-yu, WANG Xue-wen. Cyclic metallurgical process for extracting V and Cr from vanadium slag: Part II. Separation and recovery of Cr from vanadium precipitated solution [J]. Transactions of Nonferrous Metals Society of China, 2021, 31(9): 2852−2860.

[3] DASHTIAN K, GHAEDI M, SHIRINZADEH H, HAJATI S, SHAHBAZI S. Achieving enhanced blue-light-driven photocatalysis using nanosword-like VO_2/$CuWO_4$ type II n–n heterojunction [J]. Chemical Engineering Journal, 2018, 339: 189−203.

[4] KUMAR S, JAIN A, ICHIKAWA T, KOJIMA Y, DEY G K. Development of vanadium based hydrogen storage material: A review [J]. Renewable and Sustainable Energy Reviews, 2017, 72: 791−800.

[5] SKYLLAS-KAZACOS M, CAO L Y, KAZACOS M, KAUSAR N, MOUSA A. Vanadium electrolyte studies for the vanadium redox battery—A review [J]. ChemSusChem, 2016, 9: 1521−1543.

[6] YAN Yi-gang, CHEN Yun-gui, LIANG Hao, ZHOU Xiao-xiao, WU Chao-ling, TAO Ming-da, PANG Li-juan. Hydrogen storage properties of V−Ti−Cr−Fe alloys [J]. Journal of Alloys and Compounds, 2008, 454: 427−431.

[7] LIU Shi-yuan, WANG Li-jun, CHOU K. Innovative method for minimization of waste containing Fe, Mn, and Ti during comprehensive utilization of vanadium slag [J]. Waste Management, 2021, 127: 179−188.

[8] DIAO Jiang, YU Can-can, JIANG Li-yuan, LEI Jin, CHEN Lian, LI Hong-yi, XIE Bing. Oxidation behavior of vanadium and phosphorus during simultaneous vanadium extraction and dephosphorization of hot metal [J]. Metallurgical Research & Technology, 2023, 120: 501.

[9] AARABI-KARASGANI M, RASHCHI F, MOSTOUFI N, VAHIDI E. Leaching of vanadium from LD converter slag using sulfuric acid [J]. Hydrometallurgy, 2010, 102: 14−21.

[10] MOSKALYK R R, ALFANTAZI A M. Processing of vanadium: A review [J]. Minerals Engineering, 2003, 16: 793−805.

[11] YANG Han, LIU Yan, ZHANG Tian-an, LIN Sheng-nan, WANG Kun. Efficient vanadium extraction from vanadium slag by roasting-free assisted acid leaching: Pure oxygen oxidation of molten vanadium slag [J]. Metallurgical and Materials Transactions B, 2024, 55: 1231−1243.

[12] LEE J C, KURNIAWAN, KIM E Y, CHUNG K W, KIM R, JEON H S. A review on the metallurgical recycling of vanadium from slags: Towards a sustainable vanadium

production [J]. Journal of Materials Research and Technology, 2021, 12: 343−364.
[13] LIU Shi-yuan, WANG Li-jun, CHOU K. Viscosity measurement of $FeO-SiO_2-V_2O_3-TiO_2$ slags in the temperature range of 1644−1791 K and modelling by using ion-oxygen parameter [J]. Ironmaking & Steelmaking, 2018, 45: 641−647.
[14] CHEN Dong-hui, YANG Shu-de. Systematic evaluation of vanadium slag quality [J]. Hebei Metallurgy, 1993(1): 19−23. (in Chinese)
[15] TURNBULL D. Formation of crystal nuclei in liquid metals [J]. Journal of Applied Physics, 1950, 21: 1022−1028.
[16] URBAIN G, CAMBIER F, DELETTER M, ANSEAU M R. Viscosity of silicate melts [J]. Transactions and Journal of the British Ceramic Society, 1981, 80: 139−141.
[17] EINSTEIN A. A new determination of molecular dimensions [J]. Annual Physics, 1906, 19: 289−306.
[18] ROSCOE R. The viscosity of suspensions of rigid spheres [J]. British Journal of Applied Physics, 1952, 3: 267−269.
[19] KONDRATIEV A, JAK E. Modeling of viscosities of the partly crystallized slags in the Al_2O_3-CaO-"FeO"$-SiO_2$ system [J]. Metallurgical and Materials Transactions B, 2001, 32: 1027−1032.
[20] UHLMANN D R. A kinetic treatment of glass formation [J]. Journal of Non-Crystalline Solids, 1972, 7: 337−348.
[21] DIAO Jiang, XIE Bing, JI Cheng-qing, GUO Xu, WANG Yong-hong, LI Xiao-jun. Growth of spinel crystals in vanadium slag and their characterization [J]. Crystal Research & Technology, 2009, 44: 707−712.
[22] ZHOU Wang, XIE Bing, TAN Wen-feng, DIAO Jiang, ZHANG Xie, LI Hong-yi. Non-isothermal crystallization kinetics of spinels in vanadium slag with high CaO content [J]. JOM, 2016, 68: 2520−2524.
[23] EBERL D D, DRITS V A, SRODON J. Deducing growth mechanisms for minerals from the shapes of crystal size distributions [J]. American Journal of Science, 1998, 298: 499−533.
[24] KILE D E, EBERL D D, HOCH A R, REDDY M M. An assessment of calcite crystal growth mechanisms based on crystal size distributions [J]. Geochimica et Cosmochimica Acta, 2000, 64: 2937−2950.
[25] REUTER B, RIEDEL E, HUG P, ARNDT D, GEISLER U, BEHNKE J. Zur kristallchemie der vanadin (Ш)-spinelle [J]. Zeitschrift fur Anorganische und Allgemeine Chemie, 1969, 369: 306−312.
[26] LIAO Shi-ming, BO Tan-lun. Vanadium metallurgical abroad [M]. Beijing: Metallurgical Industry Press, 1985. (in Chinese)
[27] BOSI F, SKOGBY H, FREGOLA R A, HÅLENIUS U. Crystal chemistry of spinels in the system $MgAl_2O_4-MgV_2O_4-Mg_2VO_4$ [J]. American Mineralogist, 2016, 101: 580−586.
[28] ALLIBERT M, GAYE H, GEISELER J, JANKE D, KEENE B J, KIRNER D, KOWALSKI M, LEHMANN J, MILLS K C, NEUSCHÜTZ D, PARRA R, SAINT-JOURS C, SPENCER P J, SUSA M, TMAR M, WOERMANN E. Slag atlas [M]. 2nd ed. Germany: Stahlinstitut VDEh, 1995.
[29] AKAOGI M, TAJIMA T, OKANO M, KOJITANI H. High–pressure and high-temperature phase transitions in Fe_2TiO_4 and Mg_2TiO_4 with implications for titanomagnetite inclusions in superdeep diamonds [J]. Minerals, 2019, 9: 614.
[30] ERIKSSON G, PELTON A D. Critical evaluation and optimization of the thermodynamic properties and phase diagrams of the $MnO-TiO_2$, $MgO-TiO_2$, $FeO-TiO_2$, $Ti_2O_3-TiO_2$, Na_2O-TiO_2, and K_2O-TiO_2 systems [J]. Metallurgical and Materials Transaction B, 1993, 24: 795−805.
[31] ILATOVSKAIA M, SAENKO I, SAVINYKH G, FABRICHNAYA O. Experimental study of phase equilibria in the $Al_2O_3-MgO-TiO_2$ system and thermodynamic assessment of the binary $MgO-TiO_2$ system [J]. Journal of the American Ceramic Society, 2018, 101: 5198−5218.
[32] SIBANDA E T, PRINSLOO A R E, SHEPPARD C J, MOHANTY P. Size effect on magnetic properties of $MnCr_2O_4$ nanoparticles [J]. Journal of Magnetism and Magnetic Materials, 2022, 558: 169486.
[33] CAMERON M, SUENO S, PREWITT C T, PAPIKE J J. High-temperature crystal chemistry of acmite, diopside, hedenbergite, jadeite, spodumene, and ureyite [J]. American Mineralogist, 1973, 58: 594−618.
[34] THOMPSON R M, DOWNS R T. The crystal structure of diopside at pressure to 10 GPa [J]. American Mineralogist, 2008, 93: 177−186.
[35] JOHNSON W A, MEHL R F. Reaction kinetics in processes of nucleation and growth [J]. Transactions of the Metallurgical Society of AIME, 1939, 135: 396−415.

CaO 和 P_2O_5 对碱性钒渣非等温结晶行为的影响

余璨璨[1,2]，刁 江[1,2]，汪金安[1,2]，谭文奉[1,2]，李鸿义[1,2]，谢 兵[1,2]

1. 重庆大学 材料科学与工程学院，重庆 400044；
2. 重庆大学 钒钛冶金及新材料重庆市重点实验室，重庆 400044

摘 要：采用扫描电子显微镜、能量色散 X 射线光谱(SEM−EDS)和 X 射线衍射(XRD)对碱性钒渣的物相组成和显微组织进行表征；建立尖晶石结晶模型，计算碱度(CaO/SiO_2 质量比)和 P_2O_5 对碱性钒渣中各晶体的生长速率和晶体析出模式的影响；基于晶体尺寸分布(CSD)理论，研究碱性钒渣中尖晶石晶体的尺寸分布和不同温度下的生长机理。结果表明，当冷却速率为 5 K/min 时，随着温度从 1748 K 下降到 1598 K，尖晶石的平均晶粒尺寸从 12.77 μm 增加到 21.52 μm，尖晶石的生长受界面控制。随着温度从 1598 K 下降到 1548 K，尖晶石的晶粒尺寸在 1548 K 时达到 31.04 μm，尖晶石的生长受供应控制。P_2O_5 含量的增加阻碍了钒渣中晶体的生长，而碱度的增加促进了晶体的成核和生长。$MnCr_2O_4$ 在碱性钒渣中优先结晶和生长。

关键词：碱性钒渣；CaO 含量；P_2O_5 含量；尖晶石；结晶；动力学

(Edited by Xiang-qun LI)